RESEARCH ARTICLE

A baseline evaluation of oceanographic and sea ice conditions in the Hudson Bay Complex during 2016—2018

Jennifer V. Lukovich[1],*, Shabnam Jafarikhasragh[1], A. Tefs[2], Paul G. Myers[3], K. Sydor[4], K. Wong[4], Julienne C. Stroeve[1,5,6], T. A. Stadnyk[2], D. Babb[1], and D. G. Barber[1]

In this paper, we examine sea surface temperatures (SSTs) and sea ice conditions in the Hudson Bay Complex as a baseline evaluation for the BaySys 2016–2018 field program time frame. Investigated in particular are spatiotemporal patterns in SST and sea ice state and dynamics, with rankings of the latter to highlight extreme conditions relative to the examined 1981–2010 climatology. Results from this study show that SSTs in northwestern Hudson Bay from May to July, 2016–2018, are high relative to the climatology for SST (1982–2010). SSTs are also warmer in 2016 and 2017 than in 2018 relative to their climatology. Similarly, unusually low sea ice cover existed from August to December of 2016 and July to September of 2017, while unusually high sea ice cover existed in January, February, and October of 2018. The ice-free season was approximately 20 days longer in 2016 than in 2018. Unusually high ice-drift speeds occurred in April of 2016 and 2017 and in May of 2018, coinciding with strong winds in 2016 and 2018 and following strong winds in March 2017. Strong meridional circulation was observed in spring of 2016 and winter of 2017, while weak meridional circulation existed in 2018. In a case study of an extreme event, a blizzard from 7 to 9 March 2017, evaluated using Lagrangian dispersion statistics, is shown to have suppressed sea ice deformation off the coast of Churchill. These results are relevant to describing and planning for possible future pathways and scenarios under continued climate change and river regulation.

1. Introduction

In a companion paper (Lukovich et al., 2021), we examined atmospheric and river discharge conditions in the Hudson Bay Complex (HBC) from 2016 to 2018 relative to the 1981–2010 climatology as "input" to the Arctic and Northern Hemisphere Atlantic configuration of the Nucleus for European Modelling of the Ocean (NEMO)/ LIM2 ice-ocean model and the Hudson Bay System Study (BaySys). In this additional baseline study, we examine oceanographic and sea ice conditions for the same time frame, as output from the NEMO model used by all BaySys teams, to provide an understanding and estimate of changes in physical and biogeochemical processes in response to relative climate change and impacts of the regulation of river discharge. Also presented in this study is the development of an integrated observational/modeling framework based on Lagrangian dispersion statistics to characterize sea ice dynamics in the HBC.

The HBC receives water from the Canadian rivers in its watershed and, as their link to the ocean, allows for examination of freshwater-marine coupling. Arctic water enters the HBC via Hudson Strait, as well as Fury and Hecla Strait, and exits via Hudson Strait. Intrusion of Arctic water enables a transfer of Arctic conditions to lower latitudes (Ingram and Prinsenberg, 1998). Freshwater and heat budgets are central to an understanding of changes in Hudson Bay (HB), with water mass balance determined by input from Arctic waters, river discharge, and sea ice melt (Prinsenberg, 1984; Ingram and Prinsenberg, 1998; St-Laurent et al., 2012; Carmack et al., 2016). In the present study, we examine sea surface temperatures (SSTs) integral to understanding the heat budget in HB, in addition to sea ice conditions and drift in particular that contributes to

[1] Centre for Earth Observation Science, University of Manitoba, Winnipeg, MB, Canada

[2] Department of Geography, University of Calgary, Calgary, AB, Canada

[3] Department of Earth and Atmospheric Sciences, University of Alberta, Edmonton, AB, Canada

[4] Manitoba Hydro, Winnipeg, MB, Canada

[5] Centre for Polar Observation and Modelling, Earth Sciences, University College London, London, UK

[6] National Snow and Ice Data Center, University of Colorado, Boulder, CO, USA

* Corresponding author:
Email: jennifer.lukovich@umanitoba.ca

thickness and freshwater redistribution (Prinsenberg, 1988) through deformation processes, with implications for ice hazard assessments, forecasting, and resilience planning.

Previous studies have documented and evaluated observed and simulated oceanographic and sea ice conditions in the HBC (Danielson, 1971; Prinsenberg, 1986a, 1986b; Ingram and Prinsenberg, 1998; Saucier et al., 2004; Stewart and Lockhart, 2005; Hochheim and Barber, 2010; Hochheim et al., 2011; Landy et al., 2017; Jafarikhasragh et al., 2019, Ridenour et al., 2019). Prinsenberg (1986a) showed that surface temperature and salinity in the HBC increase with distance from the shoreline. Temperature (T) increases due to upwelling associated with northwesterly winds, while salinity (S) increases due to reduced impact from runoff further from shore. Regional variability in T and S (as well as sea ice variables including sea ice concentration (SIC), thickness, and drift) provides motivation for a basin-wide assessment such as is addressed by BaySys. Surface circulation in the HBC is characterized by cyclonic circulation in summer with weak coastal currents, dominant Coriolis effects, and density stratification (Prinsenberg, 1986b). Volume transport is driven by northwesterly winds in fall, and density-driven currents in response to runoff and ice melt in summer. Prinsenberg and Freeman (1986) also documented a weak diurnal signal that loses amplitude and strength with cyclonic circulation in the HB complex. Recent studies, however, have demonstrated the existence of easterly currents in southwestern HB in an anticyclonic/cyclonic configuration attributed to the combined effects of changes in seasonal river discharge associated with regulation and anticyclonic surface winds (Ridenour et al., 2019).

Previous modeling studies of sea ice dynamics in HB demonstrated that sea ice growth rates in winter are governed by ice drift and deformation in southern HB, with seasonal variations in sea ice state and dynamics and enhanced ridging in winter within a regime of high ice concentration and thickness (Saucier et al., 2004; Jafarikhasragh et al., 2019). Sea ice begins to form in northwestern HB, where it is transported to southeastern HB (Markham, 1981; Prinsenberg, 1988). Thickness distributions are due to motion of the pack ice, with ice drift speeds on the order of 10 cm/s in northwest HB and 1 cm/s in southeast HB (Stewart and Lockhart, 2005). Northwesterly winds and tidal mixing give rise to polynya formation in northwestern HB. Maximum ice cover exists in April and May, and maximum thicknesses can range from 71 cm (Moosonee) to 285 cm (Inukjuak) between February and June (Stewart and Lockhart, 2005). Also central to the HB system is the formation of landfast ice that influences freshwater-marine coupling and communication between nearshore and offshore processes. Leads form along fast ice edges with offshore winds. In mid-July, ice is no longer considered a hazard. Hochheim and Barber (2010) showed that fall freeze-up/sea ice formation begins near Week 45 until complete ice coverage, exceeding 20%–30%, in Week 48; spring breakup occurs near Week 23, with variability between years due to differences in summer and autumn winds, air temperature, cloud cover, and snow cover (Hochheim et al., 2011). Also highlighted in both studies was east–west asymmetry in SIC anomalies associated with surface winds. The importance of sea ice dynamics to the freshwater budget is illustrated by Prinsenberg (1988), who showed that an underestimation in offshore ice volume can be attributed to freshwater stored in ice ridges that can increase freshwater contributions by as much as 30%. In addition, because the magnitude of density-driven currents is proportional to the runoff rate, Prinsenberg (1983) noted that hydroelectric developments that increase winter runoff will also increase winter circulation.

In this baseline study, we examine sea ice and oceanographic conditions during the BaySys time frame using reanalysis products. In an Eulerian analysis, sea ice area (SIA), drift speed, and meridional circulation index (MCI), as defined in the next section, are evaluated for the 2016–2018 BaySys time frame relative to the 1981–2010 climatology. In a Lagrangian analysis, sea ice deformation, computed from sea ice beacons deployed near Churchill in February 2017, is examined for the impacts of March 2017 storm, characterized in Lukovich et al. (2021) by strong winds locally and high levels of precipitation regionally, based on the spatial and temporal evolution in triangular arrays.

Study objectives were thus to compare oceanographic and sea ice conditions for 2016–2018 relative to the 1981–2010 climatology and to examine the impact of the blizzard/extreme storm on sea ice dynamics in 2017 as a case study. We used standard anomaly maps, as in the companion paper on baseline atmospheric conditions (Lukovich et al., 2021), to assess spatial variability in SST and ice conditions relative to the 1981–2010 climatology (or 1982–2010 in the case of SST). Temporal changes are captured by monthly plots, while rankings depict extremes associated with SICs and drift. Definitions and methods are presented in Section 2; temporal and spatial variability in SSTs, sea ice state and dynamics in Section 3.1; and rankings in Section 3.2. The case study for the March 2017 blizzard is presented in Section 3.3, as an example of an extreme event which, in a storylines approach to describing possible future pathways and scenarios based on an assessment of a range in plausible outcomes and compound extreme events including windstorms with heavy precipitation (Shepherd et al., 2018), is relevant to climate change impact considerations and planning.

2. Data and methods

For this study, as in the companion study (Lukovich et al., 2021), the 1981–2010 time frame was selected because it (i) falls after the establishment of river discharge regulation and (ii) coincides with a climatological and conventional normal time interval established by Environment and Climate Change Canada (2020). Variables examined (and selected based on available observational and reanalysis data) include SST, SIC, and sea ice drift. Sea ice beacon observations from the BaySys field campaign were analyzed using Lagrangian dispersion statistics, including displacements in individual beacons and evolution in triangular configurations selected from an array of

beacons deployed off the coast of Churchill during the 2017 winter BaySys field campaign.

To study SST in the HBC over the baseline period (2016–2018), SST from satellite was compared with its climatology (1982–2010). We used satellite data from the Optimum Interpolation SST (OISST) Version 2 data set (Reynolds et al., 2007), which is available from the National Oceanic and Atmospheric Administration (NOAA) Earth System Research Laboratory Physical Science Division (Banzon et al., 2016). The data are available from 1982 until now, which is why the SST analysis starts in 1982. The OISST data set has been used in many climatological and modeling studies (e.g., De Szoeke and Xie, 2008; Artale et al., 2010; Singh et al., 2013; Banzon et al., 2016) due to its good temporal and spatial coverage. These are daily SST records (one daily value for each pixel), with spatial resolution of $0.25° \times 0.25°$ (approximately 25 km) based on the combination of two passive satellite data set, the Advanced Very High-Resolution Radiometer infrared satellite and Advanced Microwave Scanning Radiometer on the Earth Observing System, supplemented with SST observations from ships and buoys. Changes and bias corrections, applied to all data since the beginning of production in Version 2 of the OISST data product (as described in Banzon et al., 2016) used in the present analysis, ensure consistency in comparison between the BaySys time frame years and historical climatology.

SIC data come from the NOAA/National Snow and Ice Data Center (NSIDC) Climate Data Record of Passive Microwave Sea Ice Concentration, Version 3 (Meier et al., 2017). This data set covers the period of 1981–1987 every other day and is daily for the 1988–2018 period. The average of 2 consecutive days was used for the day missing between 2 days. Moreover, the First of March was considered as the first day of the year. The NSIDC Version 4 of the sea ice drift product (Tschudi et al., 2019) was also used in this analysis. Although the NSIDC ice drift product (25-km spatial resolution) excludes Hudson Strait and James Bay, as does the medium-resolution OSISAF ice drift product (62.5-km spatial resolution), the former provides data from 1979 to the present, whereas the latter provides data from 2006 onward. To enable comparisons for the same time frame as in the present analysis (i.e., 1981–2018), the NSIDC sea ice drift product was used. Lagrangian sea ice drift data from beacons deployed in February 2017 were further analyzed to characterize sea ice drift and deformation based on beacon triplets (following Lukovich et al., 2015; Lukovich et al., 2017), and the blizzard/extreme event in particular. Five of the 25 beacons deployed off the coast of Churchill were examined, as these instruments provided data prior to, during, and following the March 2017 storm.

Sea ice freeze-up and breakup dates in the HBC were determined according to diagnostics and criteria described in Peng et al. (2018). Day of advance is defined as the first day that SIC increases above 15% after the last summer minimum; day of closing, as the first day that SIC increases about 80% after the last summer minimum; day of opening, as the last day SIC drops below 80% before the first
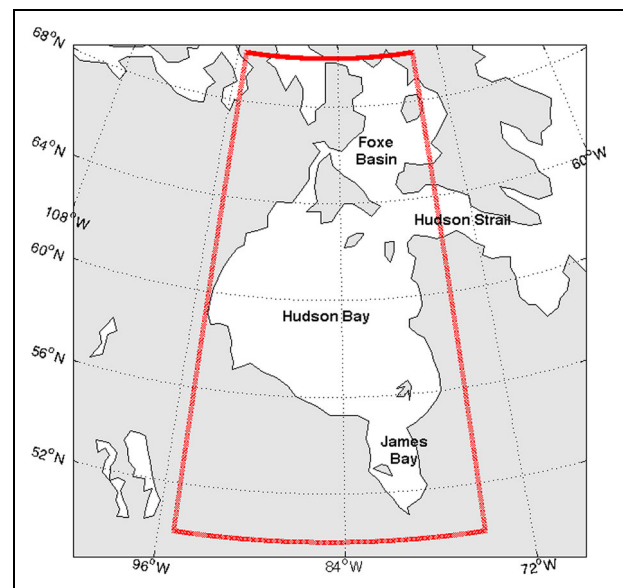

Figure 1. Map of Hudson Bay Complex and region of interest. Depicted are Hudson Bay, Hudson Strait, Foxe Basin, and James Bay. Red boundary depicts region of interest encompassing 50°–70°N and 95°–75°W. DOI: https://doi.org/10.1525/elementa.2020.00128.f1

summer minimum; and day of retreat, as the last day that SIC drops below 15% before the first summer minimum.

Standardized monthly anomalies were computed using the technique described in Lukovich et al. (2021, their Section 2) and equations provided in the Supplemental Material to illustrate spatial variability in sea ice conditions during the 2016–2018 BaySys time frame. The region of interest encompasses 50°–70°N and 95°–75°W (**Figure 1**). SIA was computed as the sum of grid cells exceeding 15% SIC (following the NSIDC convention defining 15% as the threshold between ice-covered and ice-free regions) multiplied by the SIC at each grid cell. From the NSIDC zonal (u) and meridional (v) sea ice drift components, sea ice drift speed and the MCI were analyzed as described in Francis and Vavrus (2015) and defined as

$$\text{MCI} = \frac{v|v|}{(u^2 + v^2)}$$

to characterize changes in relative zonal and meridional sea ice drift. Predominantly zonal sea ice drift is depicted by values approaching zero, while predominantly meridional sea ice drift is depicted by values approaching positive or negative one.

2.1. Lagrangian dispersion statistics

A key objective of the BaySys project was to develop an integrated observational-modeling framework for the HBC. In addition to traditional characterizations associated with model-observational data evaluation, including time series, maps of means and standard deviations, trends, and process studies that enable comparison between model output and satellite and in situ

observations from an Eulerian perspective, of interest in this study are sea ice dynamics from a Lagrangian perspective that depicts the ability of models to capture sea ice dispersion characteristics relevant for tracer and pollutant transport and mixing characterization, forecasting, and prediction. Here and in Section 3.3, we present the framework for such an evaluation using observational data for a case study of an extreme event during the BaySys field program, as a template for ongoing Lagrangian dispersion studies focused on discerning the ability of sea ice models to capture sea ice dynamics over a range of spatial and temporal scales.

In this study, we analyzed Lagrangian dispersion statistics using measurements from ice beacons deployed during the BaySys field campaigns, as outlined in Lukovich et al. (2011, 2015, 2017). Examined in particular is single-particle dispersion defined as

$$A^2 = \langle |x_i(t) - x_i(0) - \langle x_i(t) - x_i(0)\rangle|^2 \rangle,$$

for x_i, the zonal and meridional location of the ith particle/beacon in the ensemble as a function of elapsed time, t; angle brackets denote ensemble averaging. Regional-scale circulation is characterized by the scaling exponent α according to the relation

$$A^2 \sim \tau^\alpha,$$

where $\alpha = 2$ corresponds to a ballistic regime indicative of advection, $\alpha = 1$ to a diffusive regime, $\alpha = 5/3$ to an elliptic regime, $\alpha = 5/4$ to a hyperbolic regime, and $\alpha < 1$ to a subdiffusive or "trapping" regime. Single-particle dispersion was used in particular to evaluate the displacement of individual ice parcels and regional-scale structure in the sea ice drift field prior to, during, and following the March blizzard of 2017. As noted in previous studies, a ballistic dispersion regime depicts advection associated with organized structure in the ice drift field, a diffusive regime captures the behavior of particles (beacons or ice floes) that follow independent random walks, and a subdiffusive regime characterizes trapping such as would occur with dominant contributions from ice–ice interactions. A strong rotational component in the ice drift field is captured by an elliptic regime, whereas strain (shear and stretching)-dominated flow is captured by a hyperbolic regime associated with along-shear transport. Temporal scaling maps depict scaling exponent values along ice beacon trajectories for the time frame considered.

Three-particle dispersion (Prinsenberg et al., 1998; Hutchings et al., 2011; Lukovich et al., 2017) was evaluated according to the time rate of change in triplet area, A, to compute sea ice divergence, $D = \frac{1}{A}\frac{dA}{dt} = \frac{\partial u}{\partial x} + \frac{\partial v}{\partial y}$, vorticity, $V = \frac{1}{A'}\frac{dA'}{dt}$, shear, $S = \frac{1}{A''}\frac{dA''}{dt}$, and the stretching deformation rate, $N = \frac{1}{A'''}\frac{dA'''}{dt}$, where primes indicate a 90° clockwise rotation in velocity vectors. Divergence depicts changes in triangle area, vorticity in triangle orientation, and changes in shearing and stretching rates in the triangular area and shape due to distortion in the sea ice cover. Changes in sea ice motion gradients were further

characterized by relative differential kinematic parameters (DKPs), including the total deformation $D^2 + S^2 + N^2$, vorticity squared, and the Okubo–Weiss criterion $\mathrm{OW} = \mathrm{Re}\left(\frac{1}{4}\left(D^2 + S^2 + N^2 - V^2 + D\sqrt{S^2 + N^2 - V^2}\right)\right)$, which monitors relative contributions from deformation due to distortion in the sea ice cover $\mathrm{OW} > 0$, and vorticity in response to winds and inertial oscillations $\mathrm{OW} < 0$. These diagnostics were used to examine sea ice deformation prior to, during, and following the March 2017 storm as a case study in an extreme event and to improve our understanding (and, in future, model representation) of sea ice deformation response to extreme events.

3. Results
3.1. Temporal and spatial variability in oceanographic and sea ice conditions
Monthly plots of mean (spatially averaged over the HBC) standardized anomalies for SSTs, SIA, drift speed, and MCI illustrate temporal variability for the 1981–2018 time frame and differences between years during the 2016–2018 BaySys time frame. In the following, monthly plots and time series for sea ice drift speed and MCI are weighted, scaled by the number of ice-covered grid cells.

3.1.1. Oceanographic conditions
Monthly plots of SST standardized anomalies show warmer SSTs in October, November, and December from 2016 to 2018 relative to the 1982–2010 climatology (**Figure 2**). Noteworthy are sustained warmer temperatures from January to April in 2016, throughout the annual cycle in 2017, and cooler SSTs from January to September in 2018.

Maps of the 2016 monthly SST standardized anomaly relative to 1982–2010 climatology show that the maximum anomaly occurred in northern HB from May to August, while the pattern changed toward the west and center of HB during November and December (Figure S1A). This positive SST standardized anomaly represents warmer temperatures in these regions compared to its climatological value. In 2017, positive anomalies were observed around the south shores of HB in January, February, March, and April (Figure S1B). Moreover, the maximum positive anomaly occurred in July and June in the north and south of HB. Contrary to 2016 and 2017, the HBC in 2018 experienced predominantly weak or negative SST standardized anomalies, apart from a positive anomaly in June over the west side of the HB (Figure S1C). Overall, SSTs in 2016 and 2017 were warmer than in 2018 and the 1982–2010 climatology period in those particular regions.

Time series of SSTs and SST standardized anomalies further demonstrate warmer SSTs in 2017 and to a lesser extent in 2016 relative to cooler SSTs in 2018 comparable to the 1982–2010 climatology (**Figure 3**). Warmer SSTs were observed throughout the annual cycle in 2017.

3.1.2. Sea ice conditions
Monthly plots of standardized anomalies for SIA show a decline characteristic of a more heterogeneous sea ice cover in early winter over the past several
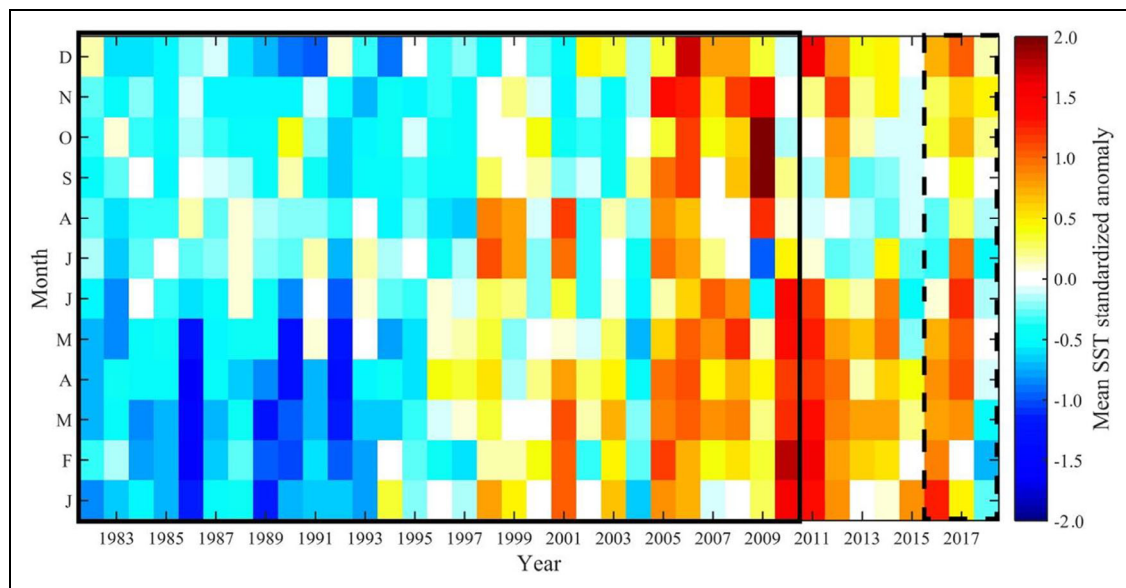
Figure 2. Monthly sea surface temperature standardized anomalies from 1982 to 2018. Monthly plots of standardized anomalies for sea surface temperature (SST) in the Hudson Bay Complex. Negative (blue) values indicate cooler SSTs for a given month than the 1982–2010 climatology, while positive (red) values indicate warmer SSTs for a given month relative to the 1982–2010 climatology. The solid rectangular perimeter depicts the 1982–2010 climatology, and the dashed rectangular perimeter the 2016–2018 BaySys time frame. DOI: https://doi.org/10.1525/elementa.2020.00128.f2
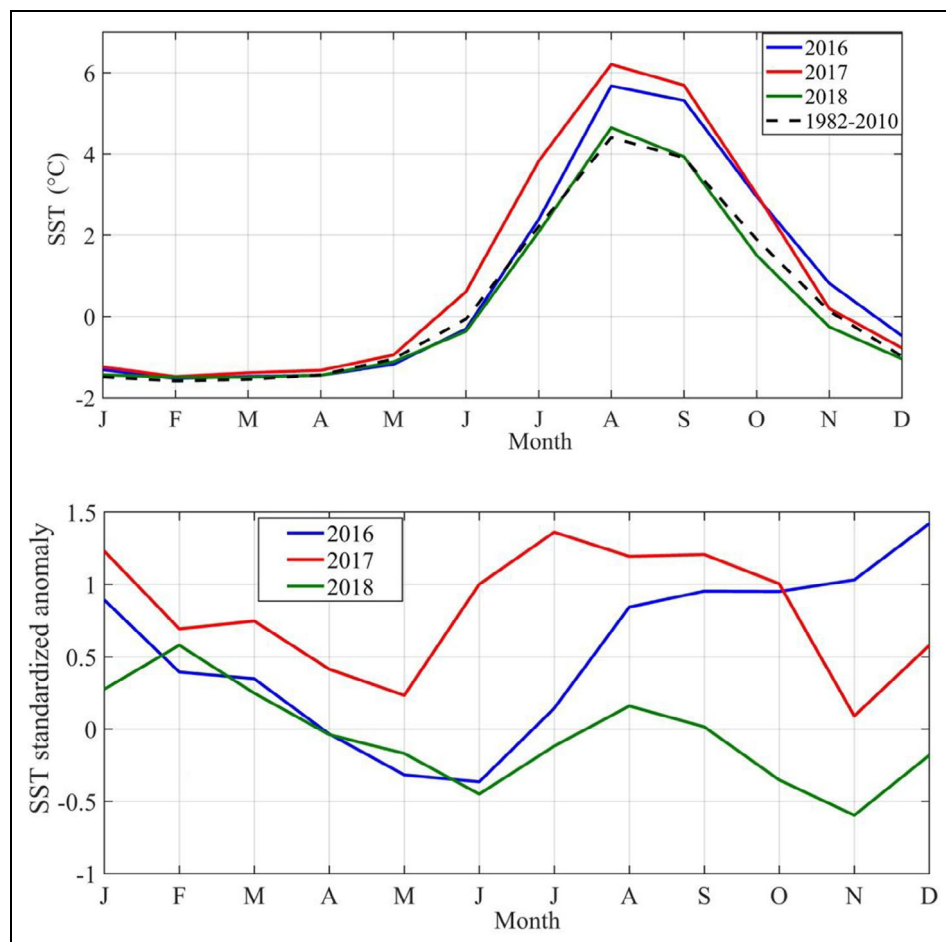

Figure 3. Mean sea surface temperature and standardized anomalies spatially averaged over the Hudson Bay Complex. Mean sea surface temperature (SST) and standardized anomalies are shown for the baseline years 2016 (blue), 2017 (red), and 2018 (green) and the 1982–2010 climatology (dashed black line). DOI: https://doi.org/10.1525/elementa.2020.00128.f3
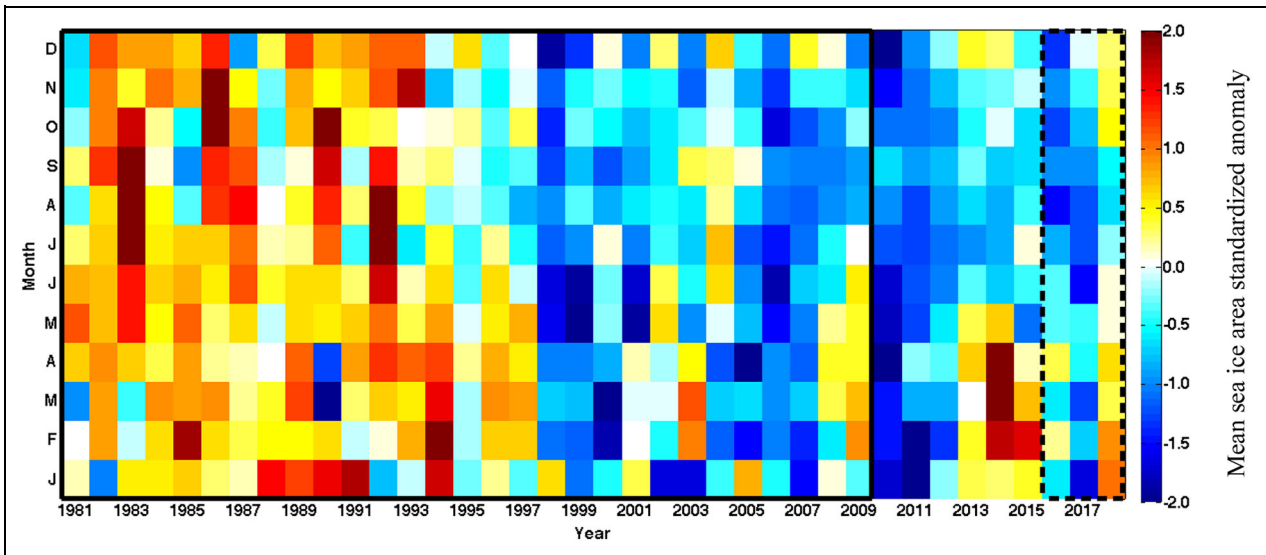
Figure 4. Monthly sea ice area standardized anomalies from 1981 to 2018. Monthly plots of standardized anomalies for sea ice area in the Hudson Bay Complex. Negative (blue) values indicate sea ice area lower than the 1981–2010 climatology, while positive (red) values indicate high sea ice area for a given month relative to the 1981–2010 climatology. The solid rectangular perimeter depicts the 1981–2010 climatology, and the dashed rectangular perimeter the 2016–2018 BaySys time frame. DOI: https://doi.org/10.1525/elementa.2020.00128.f4
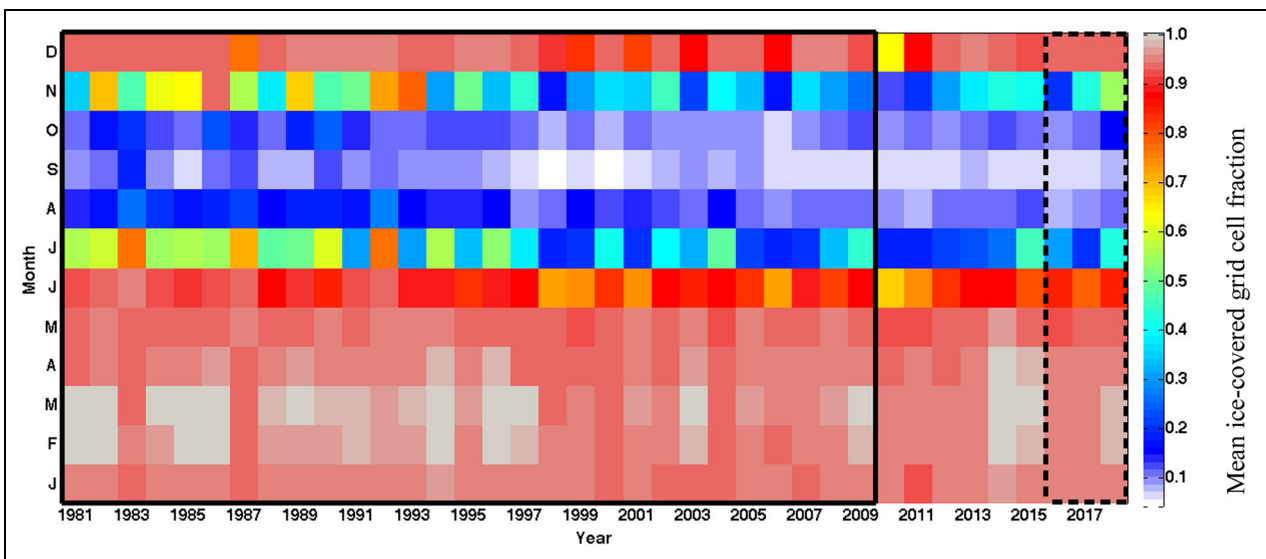
Figure 5. Monthly plot for ice-covered fraction of total grid cell number in the Hudson Bay Complex. The solid rectangular perimeter depicts the 1981–2010 climatology, and the dashed rectangular perimeter the 2016–2018 BaySys time frame. DOI: https://doi.org/10.1525/elementa.2020.00128.f5

decades (**Figure 4**). Similar plots for ice-covered fraction (defined as the ratio in the ice-covered to total number of grid cells) demonstrate enhanced variability and reduced ice coverage during the transition months of June and November (**Figure 5**) for the entire time frame. Predominantly negative SIA standardized anomalies characterize 2016 and the full annual cycle in 2017, while positive SIA standardized anomalies characterize the winter months in 2018 (**Figure 4**). Enhanced (reduced) mean drift speed is observed in December (January) for 2016, 2017, and 2018 (**Figure 6**). Weakened meridional sea ice circulation characterizes December 2016 and 2018 (**Figure 7**).

Contrasting MCI anomalies in May of 2016 and 2017, as well as in January and to a lesser extent December of 2017 and 2018, also reflect the contrasting sea level pressure (SLP) anomalies during the BaySys time frame (Lukovich et al., 2021, their figure 1).

Higher SIA standardized anomalies despite warmer SSTs in October, November, and December (**Figures 2** and **4**) can be attributed to early ice advance (as is shown below) due to colder surface air temperatures in September, October, and November of 2018 (Lukovich et al., 2021, their figure 16). Larger SIA standardized anomalies for January, February, and March of 2018 can be
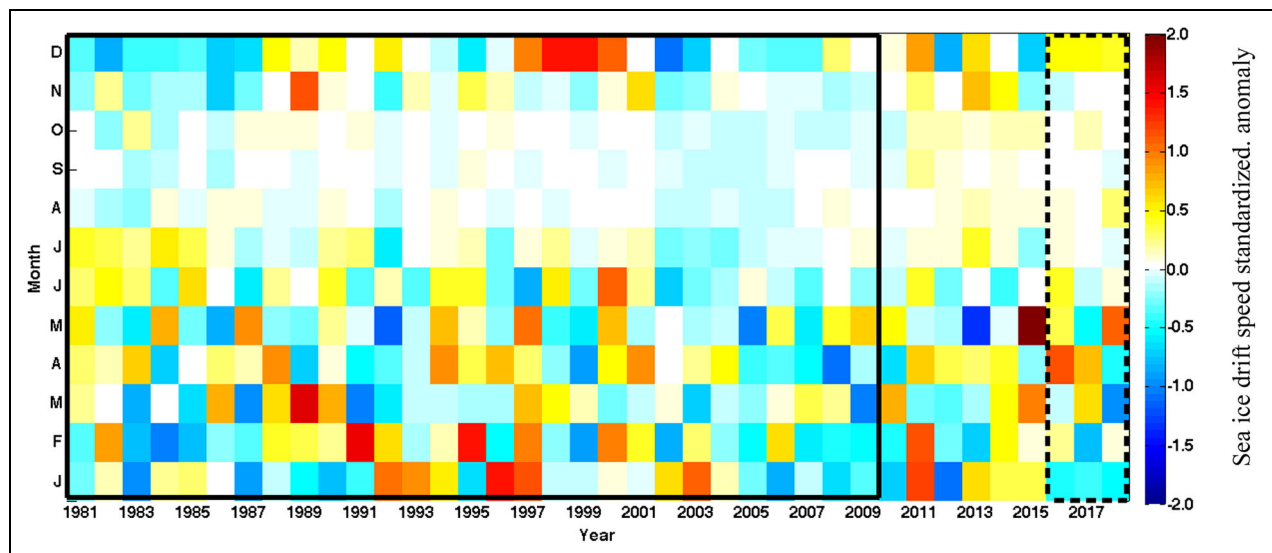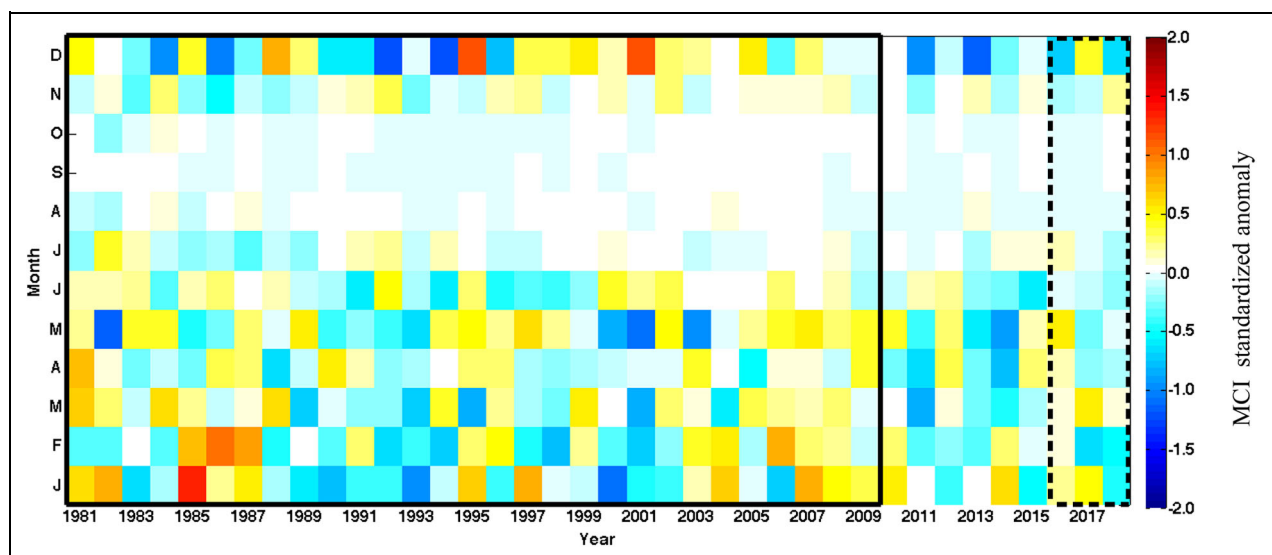
Figure 6. Monthly plots of standardized anomalies for sea ice drift speed in the Hudson Bay Complex. Standardized anomalies were weighted by the number of ice-covered grid cells, as depicted by the ice cover fraction shown in **Figure 5**. The solid rectangular perimeter depicts the 1981–2010 climatology, and the dashed rectangular perimeter the 2016–2018 BaySys time frame. DOI: https://doi.org/10.1525/elementa.2020.00128.f6

Figure 7. Monthly plots of standardized anomalies for the meridional circulation index in the Hudson Bay Complex. Negative values for the absolute meridional circulation index (MCI) indicate reduced meridional drift, and positive values indicate enhanced meridional drift relative to the 1981–2010 climatology. The solid rectangular perimeter depicts the 1981–2010 climatology, and the dashed rectangular perimeter the 2016–2018 BaySys time frame. DOI: https://doi.org/10.1525/elementa.2020.00128.f7

attributed, however, to cooler than normal SSTs (**Figures 2** and **4**).

Maps of standardized anomalies for monthly SIC further demonstrate regional differences in SIC during the 2016–2018 BaySys time frame (Figure S2A–C). Northwest HB is characterized in all 3 years by unusually high SIC in February; and in 2017 (2016 and 2018) by low (high) SIC in March relative to the 1981–2010 climatology. Comparatively high SIC was also observed in eastern HB in April and May of 2016 and 2018. Anomalously low SIC occurred throughout the basin from July to December of 2016 and

in northwestern HBC in particular in November. In 2017, anomalously low SIC occurred throughout the HBC in January, March, and June to August; in 2018, in western HBC in a manner consistent with high SSTs in June.

Figure 8 shows the month when sea ice started to decrease and SIC dropped below 80% based on day of opening. The climatology map shows that sea ice started to open in May in the north and east of HB and north of Hudson Strait prior to the opening in the southwest and center of Foxe Basin, which tended to occur in late June. In general, the baseline years 2016–2018 follow the same
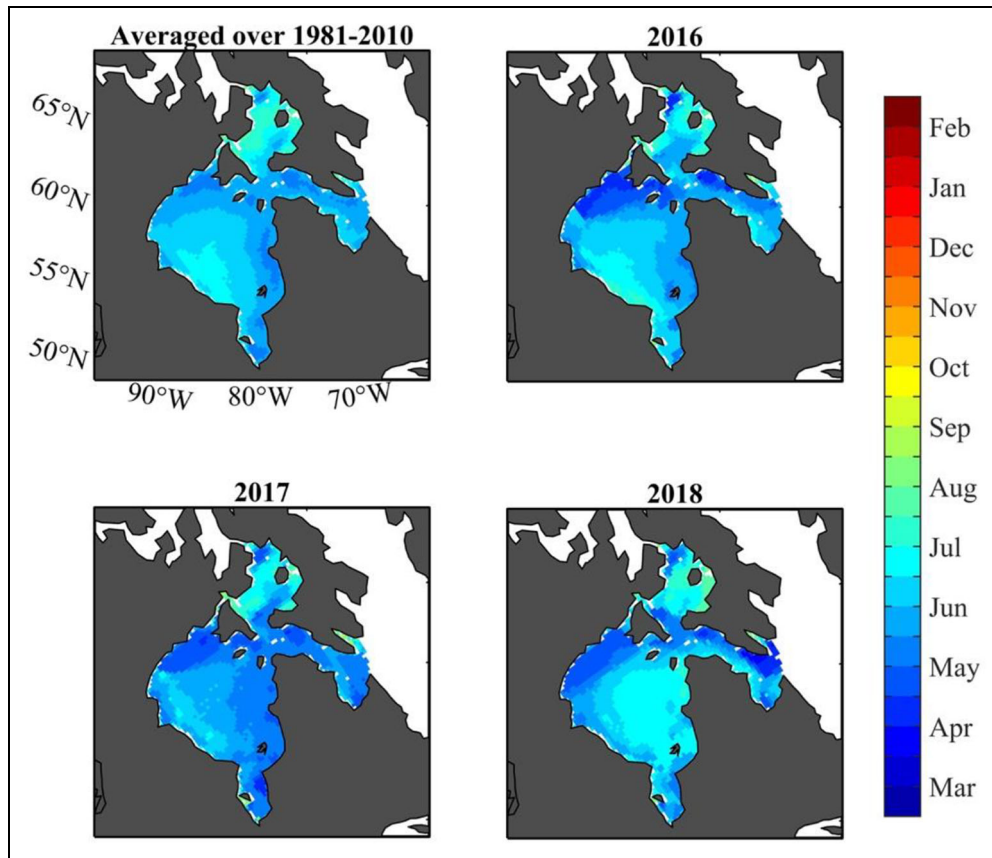
Figure 8. Day of opening for 1981–2010 climatology and 2016–2018 baseline years in the Hudson Bay Complex. Day of opening (color-coded by month) was computed using National Oceanic and Atmospheric Administration/National Snow and Ice Data Center Climate Data Record of Passive Microwave Sea Ice Concentration, Version 3. DOI: https://doi.org/10.1525/elementa.2020.00128.f8

pattern as the 1981–2010 climatology except in the east of HB in 2018 when, in contrast to other years, the ice started to break up later than in western HB. This later breakup is in keeping with the unusually high SIA in February of 2018 (**Figure 4**). The same regimes and patterns for day of opening also pertain to sea ice retreat (Figure S3). SIC started to decrease below 15% sooner over the north and west of HB in the climatology and in all baseline years except in eastern HB in 2018.

SIC for the 1981–2010 climatology started to increase and exceed the 15% threshold in late September and October in Foxe Basin and in late October and early November in northwest HB (**Figure 9**). This pattern is similar for all years, although the time for sea ice advance happens later in 2016 (early December). The pattern for sea ice closing (when SIC exceeds the 80% threshold) is consistent with that for sea ice advance (Figure S4). Sea ice started to close in late November. Again, this time is later for 2016 (late December).

Maps of standardized anomalies for monthly sea ice drift speed highlight regional variability in sea ice dynamics during the BaySys time frame (Figure S5A–C). In 2016, enhanced drift was observed adjacent to regions with unusually low SICs, including in western HBC in February and April, southeastern HBC in June, and northern HBC in December (Figure S5A). In 2017, enhanced sea ice drift

speeds are found in lower SIC regimes in southeastern HBC in March, as well as northwestern HBC in April and November. Higher ice drift speed and SIC in northwestern HBC in December coincide spatially with gradients in anomalous SLP high and low regimes (Lukovich et al., 2021, their figure S1B, last panel) that would contribute to ice advection in this region (Figure S5B). In 2018, high ice drift speed anomalies in western HB in February and May are found in the vicinity of anomalously low SIC regimes (Figure S5C) during anomalously low SLP and windy atmospheric conditions (Lukovich et al., 2021, their figure 16).

Noteworthy are unusually high ice drift speeds in the HBC in March and April 2017 when unusually high river discharge occurred (Figure S5B; Lukovich et al., 2021, their figure S9). High ice drift speeds were also observed in February and April 2016 during a year characterized by high discharge in January and March. These results are consistent with the study by Prinsenberg (1983) showing enhanced sea ice circulation in response to increased runoff from hydroelectric developments in winter.

Standardized anomalies for the absolute value of the MCI as a measure of changes in meridional circulation in the HBC further highlight regional differences in circulation from 2016 to 2018 (Figure S6A–C). In this figure, enhanced (reduced) meridional circulation is depicted by
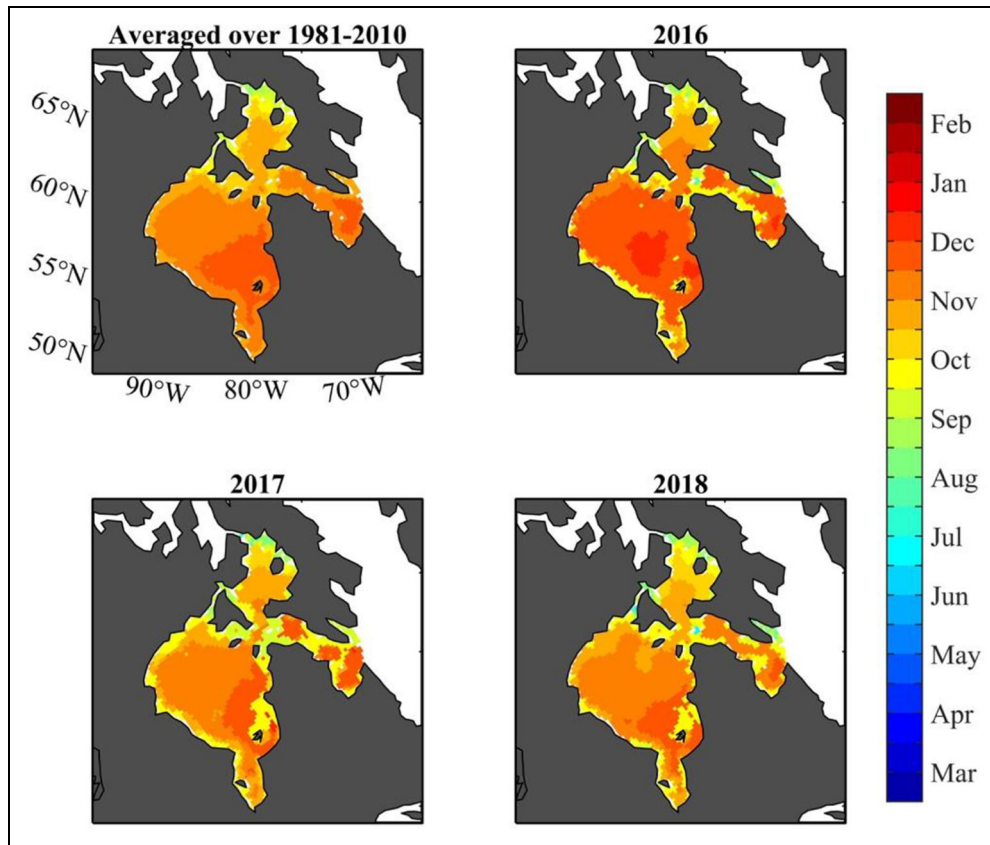
Figure 9. Sea ice day of advance for 1981–2010 climatology and 2016–2018 baseline years. Day of opening (color-coded by month) was computed using National Oceanic and Atmospheric Administration/National Snow and Ice Data Center Climate Data Record of Passive Microwave Sea Ice Concentration, Version 3. DOI: https://doi.org/10.1525/elementa.2020.00128.f9

positive (negative) anomaly values. In 2016, meridional circulation was enhanced in a lower SIC and higher sea ice drift regime in March and reduced in December characteristic of predominantly zonal flow. Similar behavior is observed in 2018, while the opposite occurred in 2017.

Time series of sea ice breakup and freeze-up, SIA, drift speed, and MCI with their standardized anomalies further demonstrate differences between years during the 2016–2018 time frame (**Figures 10–13**). To identify precise spatially averaged dates associated with the sea ice breakup and freeze-up patterns in **Figures 8** and **9**, the time series of days of opening, retreat, advance and closing are shown in **Figure 10**. The minimum SIC (day of retreat) happened earlier for baseline years of 2016 (Day 235) and 2017 (Day 242) compared with climatology (Day 244). Also, sea ice started to increase above 15% (day of advance) later for these years (Days 288 and 276, respectively) compared to climatology (Day 274). Year 2018 shows dates for sea ice retreat and advance that are similar to climatology.

Lower than normal (relative to the 1981–2010 climatology) SIA values are observed during spring months of 2016, with enhanced variability defined according to maximum and minimum SIA during the 1981–2018 time frame observed during spring and early winter (**Figure 11**). Anomalously high SIA is observed in 2018.

Standardized anomalies for sea ice drift speed show lagged extrema in winter and high ice drift speeds in March of 2017 relative to 2016 and 2018 (**Figure 12**). Also of interest are low ice drift speeds due to low ice cover in November 2016 that yield standardized anomaly results comparable to 2017 and 2018. Time series for the MCI show enhanced meridional circulation in December 2017 compared to 2016 and 2018. Mean meridional sea ice circulation was enhanced in March during the extreme blizzard event and suppressed in April of 2017 following that storm (**Figure 13**).

In summary, 2016 was an unusually warm year (relative to the 1981–2010 climatology), with lower than normal SIA during winter, as well as higher (lower) than normal freshwater discharge to the HBC in winter (summer) months. In addition, 2018 was a predominantly cold and windy year, with higher than normal SIA in January and February, as well as low discharge to the HBC in May and June and from September to December. Furthermore, 2017 was characterized by a low in SLP and highs in temperature and precipitation in January and intermittent high and low wind events compared to the 1981–2010 climatology, with lower than normal SIA, unusually high zonal ice drift in April, as well as unusually high discharge in March and April and low discharge (high meridional ice drift) to the HBC in September.
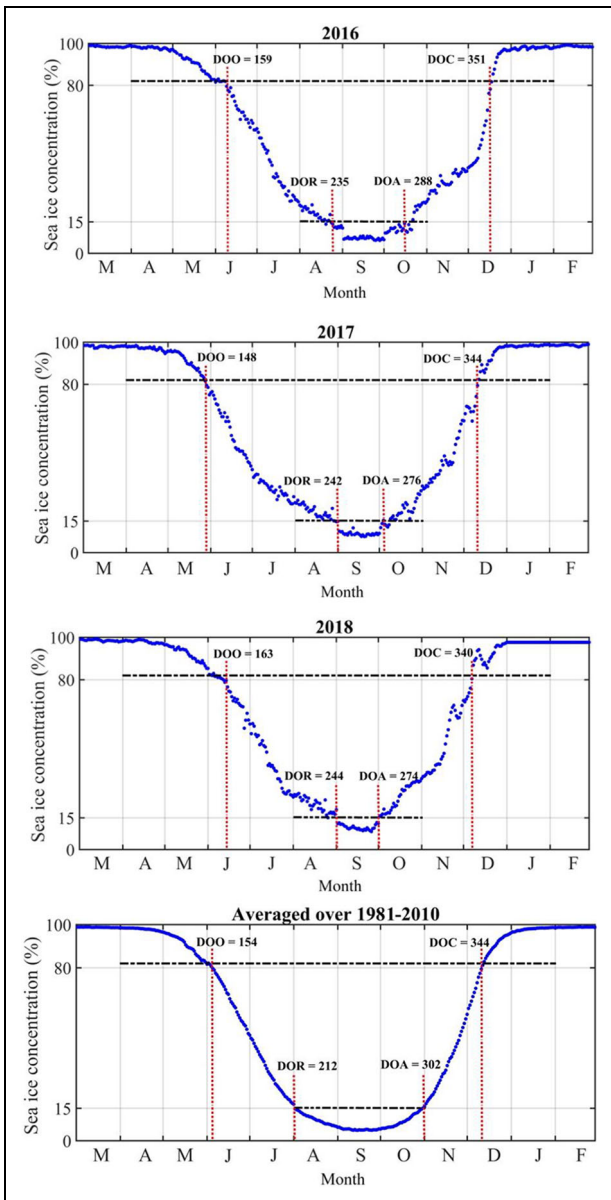
Figure 10. Time series of sea ice concentrations in Hudson Bay Complex for baseline years and climatology. Baseline years are 2016–2018; climatology is averaged over 1981–2010. Following Peng et al. (2018), horizontal black lines indicate thresholds for defining breakup and freeze-up dates; vertical red lines indicate day of onset (DOO), day of retreat (DOR), day of advance (DOA), and day of closing (DOC). DOI: https://doi.org/10.1525/elementa.2020.00128.f10

3.2. Rankings and extreme sea ice conditions

Ranking the sea ice variables of SIA, drift speed, and MCI, spatially averaged over the HBC for the 1981–2018 time frame, highlights whether a particular month or season during the BaySys baseline 2016–2018 time frame is characterized by extreme sea ice conditions (**Figures 14** and **15**). Both figures provide a synopsis of the monthly plots presented in the previous section.

Rankings show that the HBC is characterized by low SIA during the winter months (December–February) of

2016–2017, which was partially restored in 2017–2018. High ice drift speeds are observed in December of 2016, 2017, and 2018, with enhanced meridional circulation observed in December of 2017. In consideration of only extreme events (**Figure 15**), low (high) SIA is observed in winter 2016/2017 (2017/2018), while low SIA coincides with high SLP regimes in fall/late summer in 2016 and 2017. High ice drift speeds coincide with strong winds in April of 2016; low (high) ice drift speeds are found in February (April) of 2017, which may be attributed to low SIA following the March blizzard and high SSTs in March and April. Low ice drift speeds occurred following unusually high SIA in winter of 2018, while high ice drift speeds coincided with windy conditions in May and August of 2018. Rankings also show weakened meridional circulation in April of 2017 following the March 2017 blizzard, enhanced meridional drift in December of 2017, and sustained reduced meridional circulation in winter of 2018.

3.3. Lagrangian dispersion statistics
3.3.1. A case study in extremes: Ice drift beacons and the blizzard/wind storm of winter 2017

As noted by Lukovich et al. (2021), the March 2017 blizzard within the HBC was captured by the compound extreme event of strong winds with heavy precipitation. In this section, we apply concepts from Lagrangian dispersion statistics to observational data recorded by ice drift beacons deployed off the coast of Churchill during the BaySys winter field campaign in 2017 (**Figure 16**, left panel). Single-particle dispersion is used to identify organized structure in the ice drift field and sea ice dynamical regimes, while three-particle dispersion is used to characterize sea ice deformation (changes in sea ice motion gradients) before, during, and following the blizzard and extreme event of March 7–9, 2017, near Churchill, Manitoba.

Ice beacon trajectories from February to March exhibit recirculation patterns and loops beyond the 50-m contour superimposed upon regional-scale cyclonic circulation (**Figure 16**, right panel). Specifically, beacons launched on February 4 and located near 93°W, 59°N on February 10 traveled northwest until the end of February and subsequently southeast until March 20 in a cyclonic circulation pattern. Superimposed on this regional scale feature are smaller-scale "loops," in the vicinity of the symbols depicting the storm onset near 94°W, that ensued during the storm, after which the beacons continued their regional-scale cyclonic circulation southeast.

Evolution in these trajectories is captured by single-particle dispersion (**Figure 17**, left panel), or the displacement of the beacons from their origin, which in this case lies at the coordinates associated with February 10 (**Figure 16**, right panel). In particular, total dispersion is characterized by predominantly meridional dispersion or displacements until approximately February 19, then zonal dispersion until March 11, after which meridional dispersion dominates as trajectories continue southeast. Also noteworthy are the limited total (zonal) displacements from February 22 to storm onset on March 7, and the sharp decrease in meridional displacements during the storm, characteristic of loops associated with ice-ice and
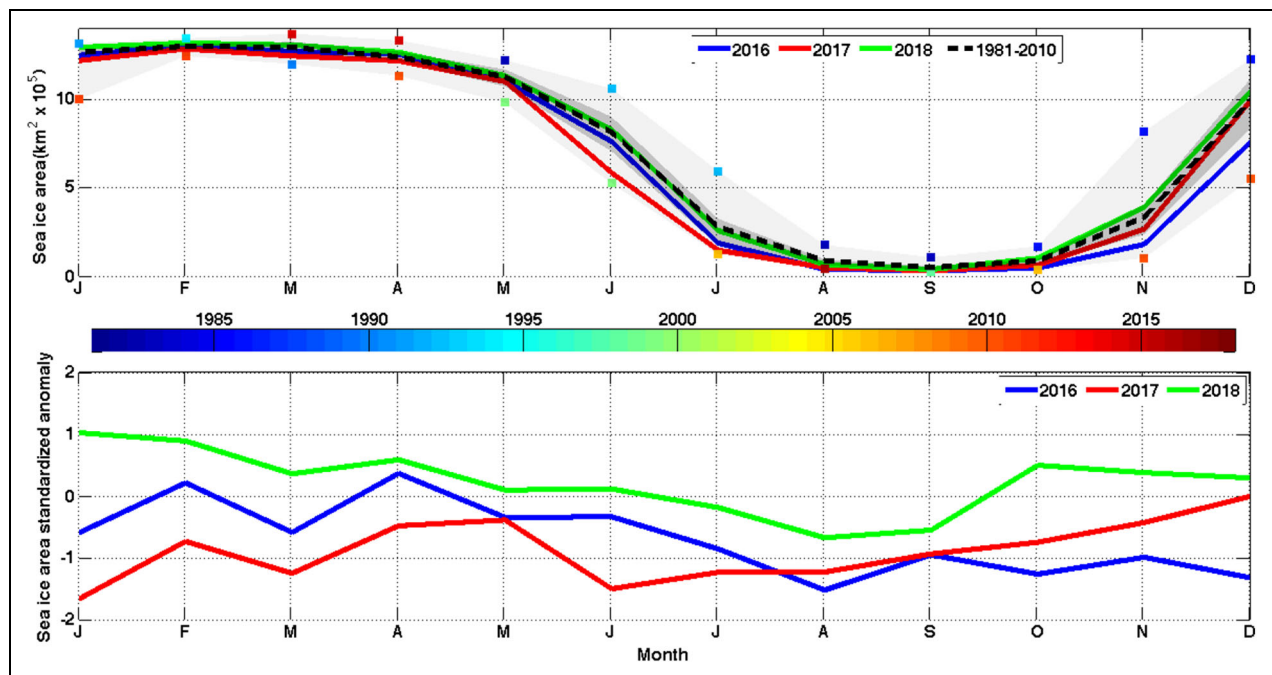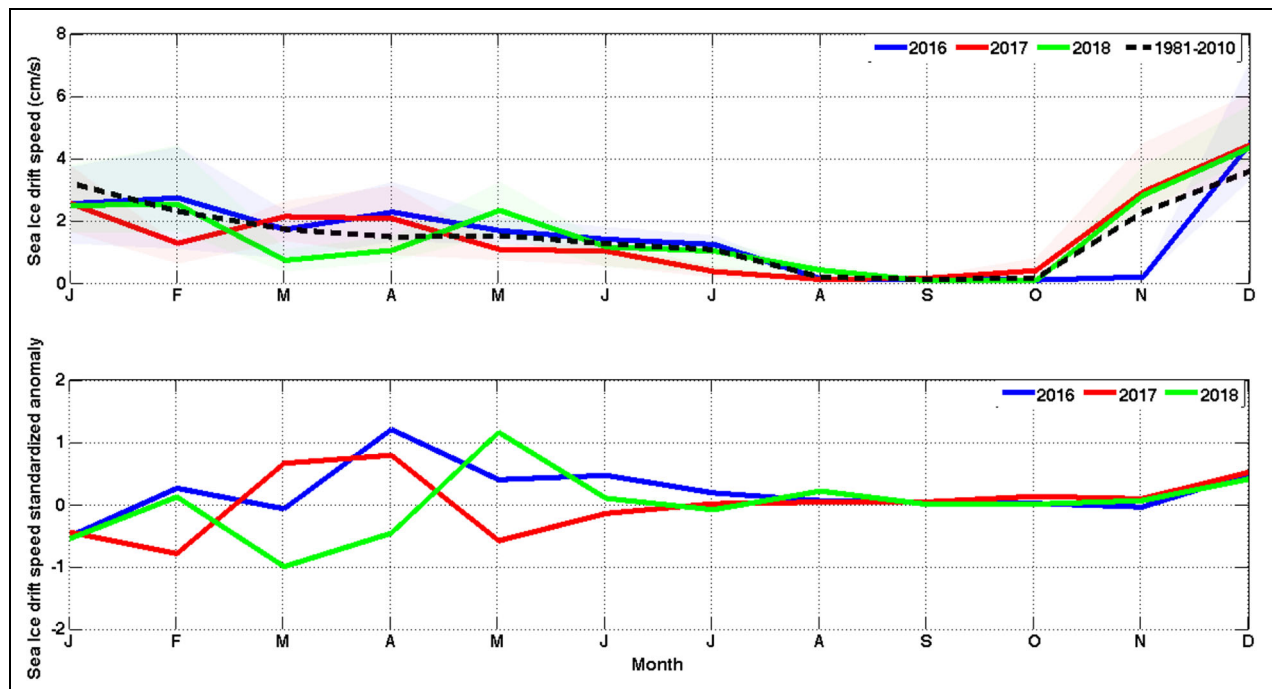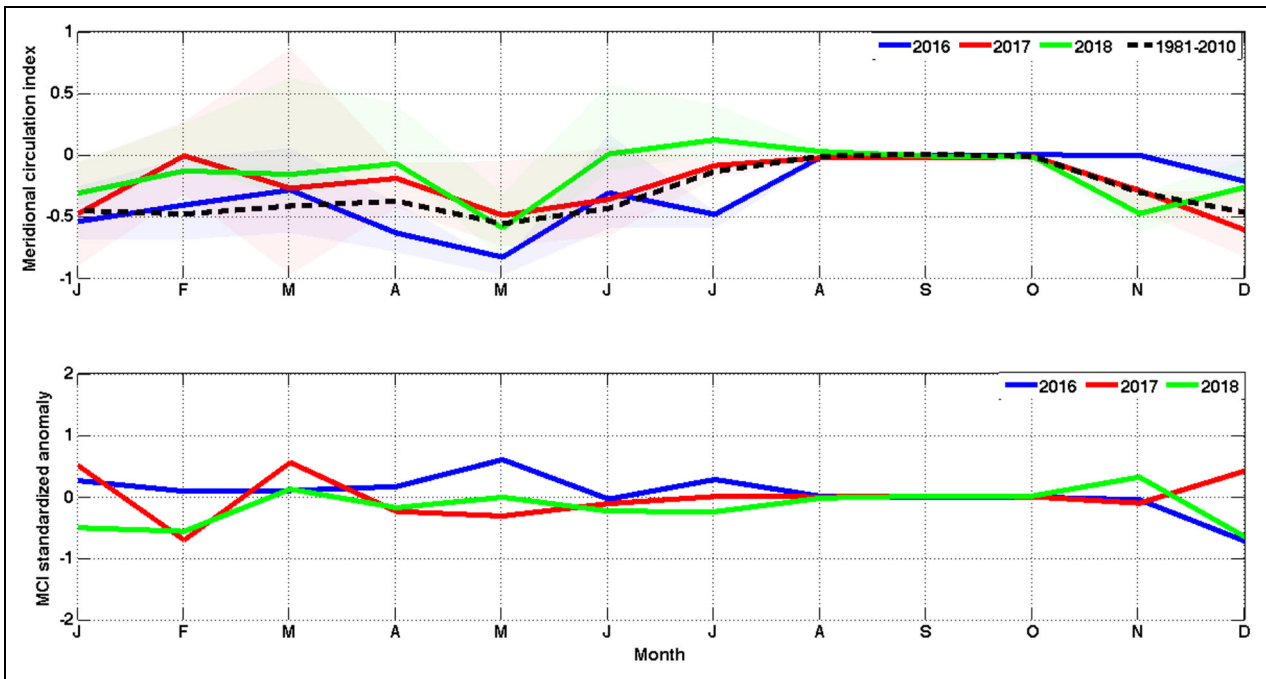
Figure 11. Time series of sea ice area in Hudson Bay Complex for baseline years and climatology. Baseline years of 2016–2018 are the solid color-coded lines; climatology averaged over 1981–2010 is the dashed black line, for times series of sea ice area. Dark shading depicts the interquartile range; light-shading, the range between maximum and minimum values for the 1981–2018 time frame. Colored symbols depict year (on color bar) when maximum and minimum sea ice values occurred (upper panel). Standardized anomalies for monthly sea ice area relative to climatology are also shown (lower panel). DOI: https://doi.org/10.1525/elementa.2020.00128.f11

Figure 12. Time series of ice drift speed in Hudson Bay Complex for baseline years and climatology. Baseline years of 2016–2018 are the solid color-coded lines; climatology averaged over 1981–2010 is the dashed black line. Shading depicts the interquartile range to demonstrate spatial variability in weighted sea ice drift speeds (calculated as in Lukovich et al., 2021). Standardized anomalies for monthly ice drift speed relative to climatology are also shown (lower panel). DOI: https://doi.org/10.1525/elementa.2020.00128.f12

Figure 13. Time series of meridional circulation index in Hudson Bay Complex for baseline years and climatology. Baseline years of 2016–2018 are the solid color-coded lines; climatology averaged over 1982–2010 is the dashed black line. Shading depicts the interquartile range to demonstrate spatial variability in the meridional circulation index (MCI). Standardized anomalies for MCI relative to climatology are also shown (lower panel), where positive (negative) values indicate enhanced (reduced) meridional sea ice drift. DOI: https://doi.org/10.1525/elementa.2020.00128.f13
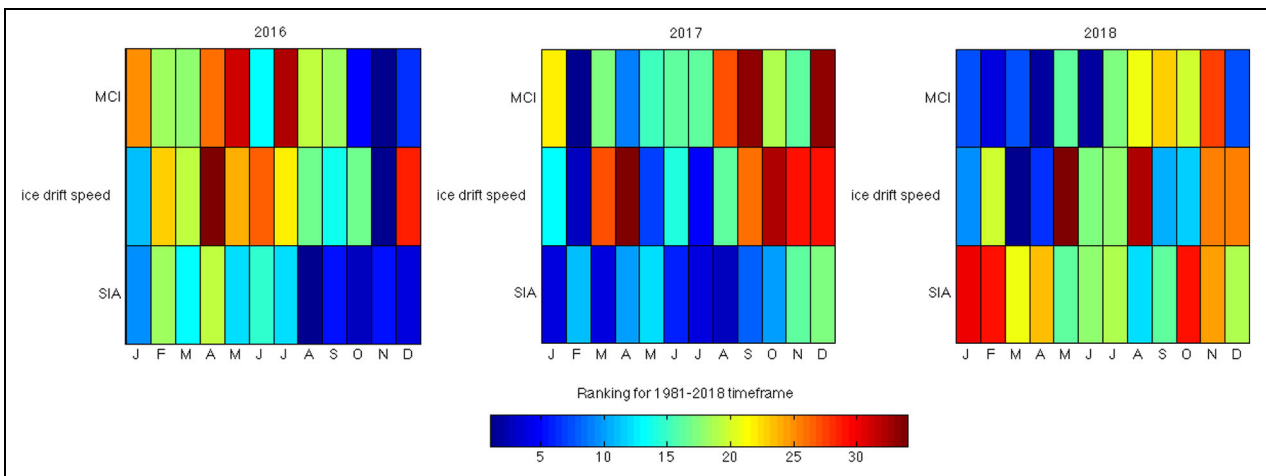
Figure 14. Rankings for sea ice area, drift speed, and meridional circulation index for 2016–2018 BaySys time frame. Depicted are monthly rankings for sea ice area, drift speed, and meridional circulation index (MCI) for 2016–2018 BaySys time frame. Ranking is in ascending order: low (blue) values indicate lower sea ice area (SIA) and drift speed and weaker meridional sea ice circulation (MCI), while high (red) values indicate higher SIA and drift speed and stronger MCI than during the 1981–2018 time frame. DOI: https://doi.org/10.1525/elementa.2020.00128.f14

ice-coast interactions resulting in displacements in the zonal direction in response to strong winds encountered during the storm. Total and meridional dispersion equilibrate following the storm, indicating limited displacement in the beacon trajectories.

Temporal scaling maps based on slopes and the transition regimes depicted in single-particle dispersion for observed ice beacon trajectories show the evolution in sea ice dynamical regimes prior to, during, and following the

March 7–9, 2017, blizzard (**Figure 17**, right panel). Before the storm, the temporal scaling map shows scaling exponent values of $\alpha \sim 1.7 \sim {}^{5}/_{3}$ and $\alpha \sim 3$ characteristic of elliptic and super-diffusive regimes until February 22, followed by a subdiffusive regime, $\alpha < 1$, until March 3 and meridional (southward) advection. During the storm, sea ice dispersion is characterized by a subdiffusive regime. Following the storm, sea ice dispersion is captured by combined super- ($\alpha > 1$) and subdiffusive regimes,
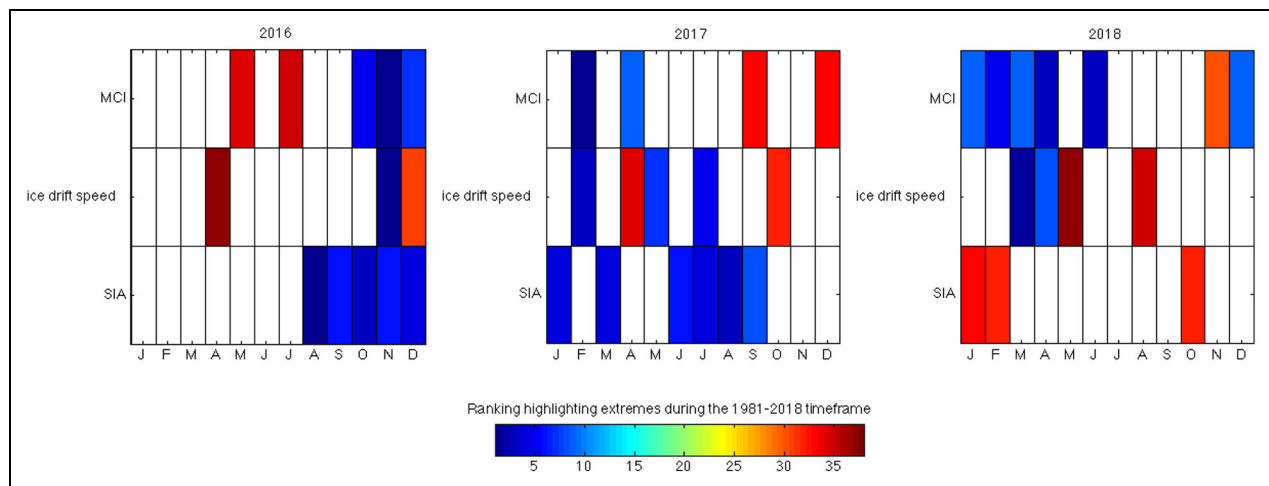
Figure 15. Rankings of extreme conditions in sea ice variables for the 2016–2018 BaySys time frame. These monthly rankings show only values for sea ice area (SIA), ice drift speed, and meridional circulation index (MCI) that lie outside of the upper and lower quartiles for conditions averaged over the 1981–2018 time frame. Blue values indicate extreme lows; red values indicate extreme highs. DOI: https://doi.org/10.1525/elementa.2020.00128.f15
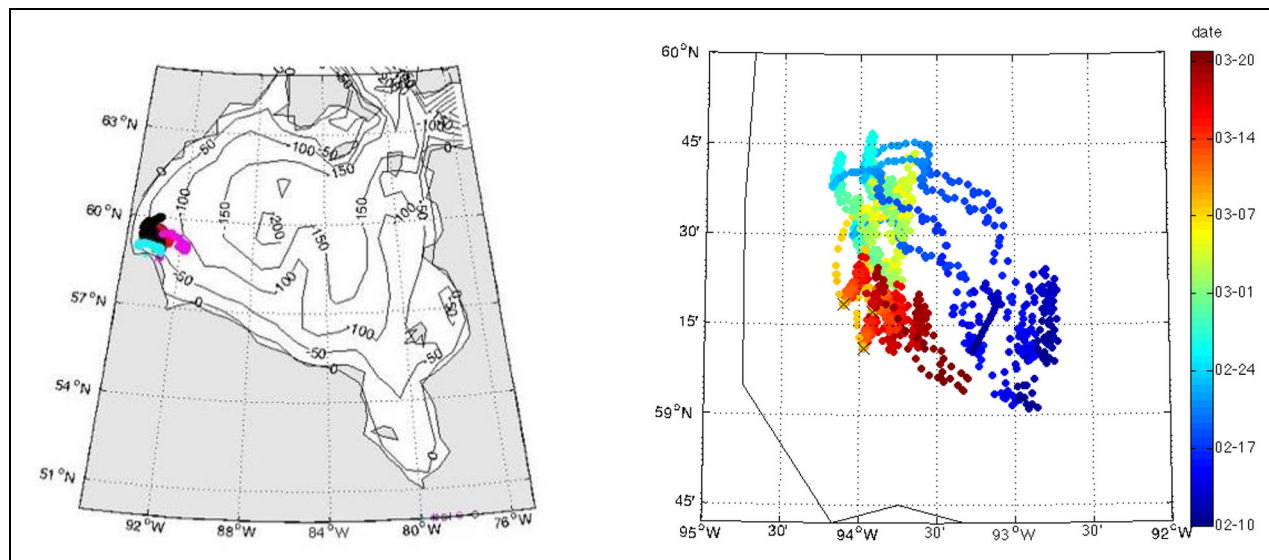

Figure 16. Ice beacon trajectories during the winter 2017 BaySys field campaign. Ice drift beacons (a) deployed near Churchill on February 2 (separate colors for each beacon); and (b) trajectories as a function of date (color bar) beginning on February 10 and thus before, during, and after the blizzard of March 7–9, 2017. Recirculation patterns exist beyond the 50-m contour shown in (a); transport is governed by cyclonic circulation and loops shown in (b). DOI: https://doi.org/10.1525/elementa.2020.00128.f16

characteristic of trapping and flight events and ice–ice and ice–coast interactions (**Figure 17**, right panel). In summary, sea ice dispersion is described by elliptic and super-diffusive dynamical regimes characteristic of inertial oscillations superimposed on ice–ice, ice–coast interactions, and nonlocal transport before the storm; a subdiffusive dynamical regime and "trapping" during the storm; and trapping and flight events and suppressed displacements characteristic of predominantly local interactions following the storm.

Investigation of sea ice deformation is based on triplet area and DKPs, including divergence, vorticity, shearing deformation rate, and stretching deformation rate

(**Figures 18** and **19**). Before the storm (in early and late February), vorticity and the shearing deformation rate contribute to sea ice deformation, which we speculate can be attributed to the combined effect of inertial oscillations depicted by vorticity and the elliptic regime, and shearing due to interactions between mobile and landfast ice with the coastline. DKPs show weak deformation, evident in vanishing values during and following the March 7–9 blizzard, which may be an artifact of what is referred to as healing in Bouillon and Rampal (2015), whereby leads and cracks in the ice cover refreeze due to cold temperatures and consolidation in the ice cover. Temperatures during the blizzard decreased by approximately 10°C.
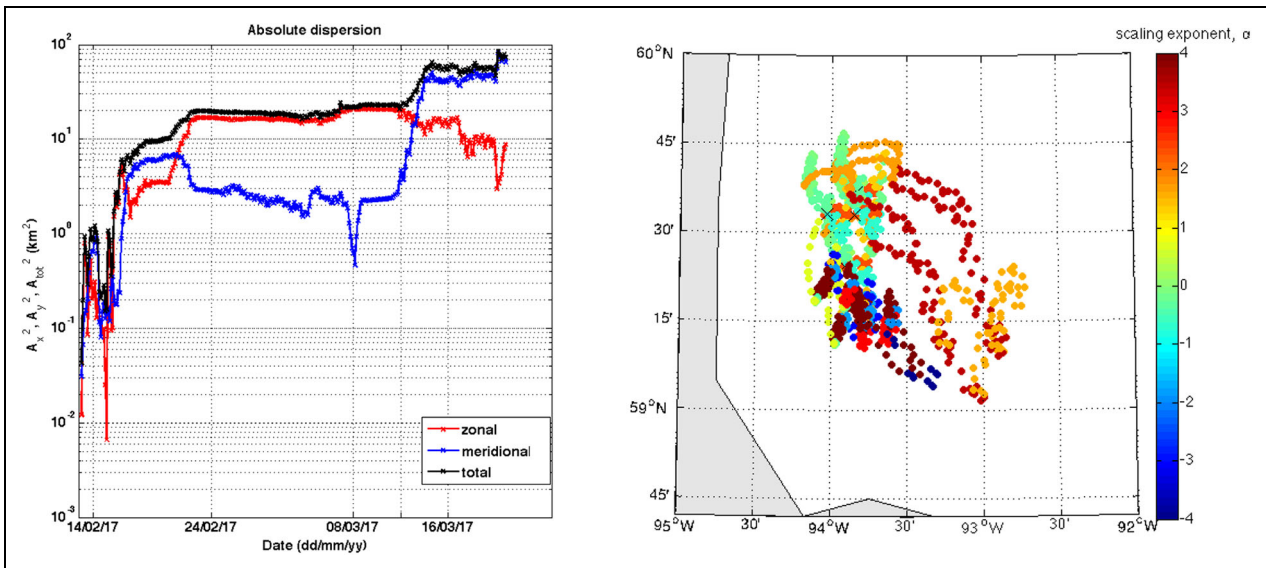
Figure 17. Single-particle dispersion statistics and temporal scaling for ice beacon trajectories during the winter 2017 blizzard. Absolute dispersion statistics showing zonal, meridional, and total displacements (left panel) and temporal map (right panel) of scaling exponent values (color bar) derived from total absolute dispersion before, during, and after the March 7–9 blizzard. DOI: https://doi.org/10.1525/elementa.2020.00128.f17
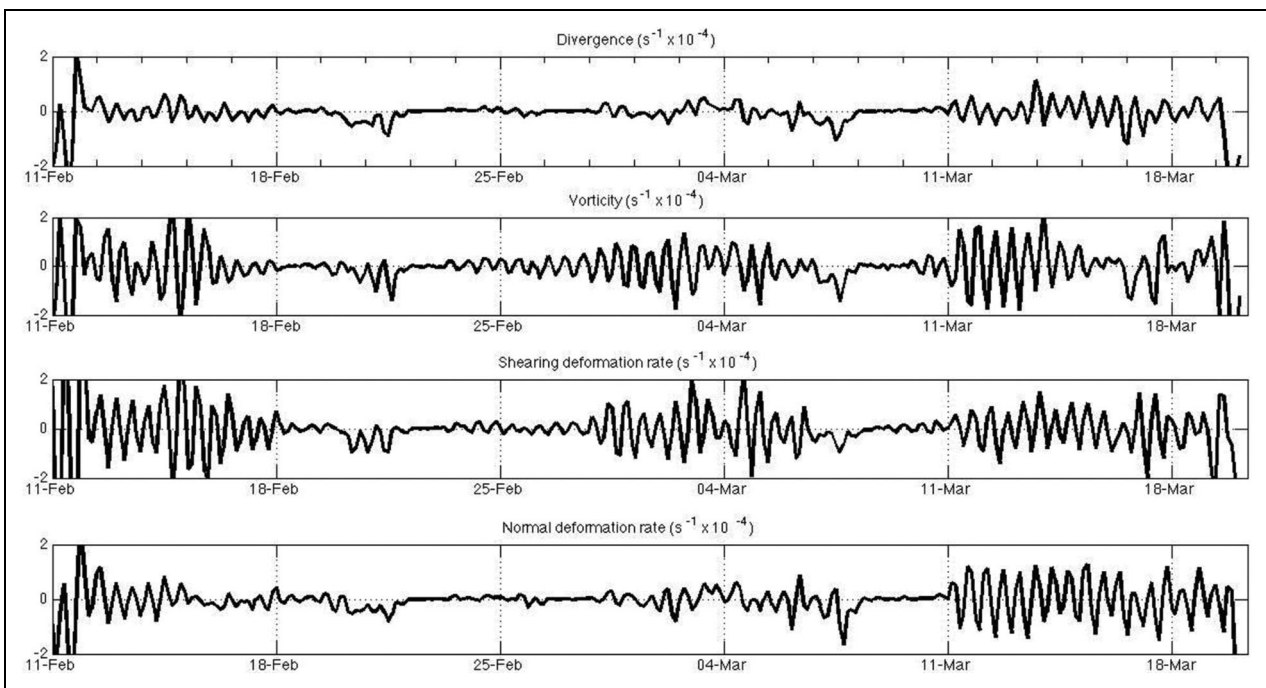

Figure 18. Sea ice deformation before, during, and after the extreme blizzard event of March 7–9, 2017. Sea ice deformation parameters shown are (top to bottom) sea ice divergence, vorticity, shearing deformation rate, and normal deformation rate. Please see the text for more details on the determination of these parameters. DOI: https://doi.org/10.1525/elementa.2020.00128.f18

Following the storm, increased frequency in stretching rate oscillations captures elongation in the triangular configuration characteristic of filamentation in the sea ice cover, which accompanies a return to enhanced vorticity and shearing deformation rates. Relative DKPs further illustrate a decline in total ice deformation during and following the storm that is recovered after March 11. Also

of interest are more subtle changes in the sea ice vorticity squared during the storm that are manifested as vanishing Okubo–Weiss values, indicating comparable contributions from total sea ice deformation and vorticity during this blizzard, preceded by predominantly shear and vorticity events and followed by alternating predominant contributions from vorticity and shear and stretching rates
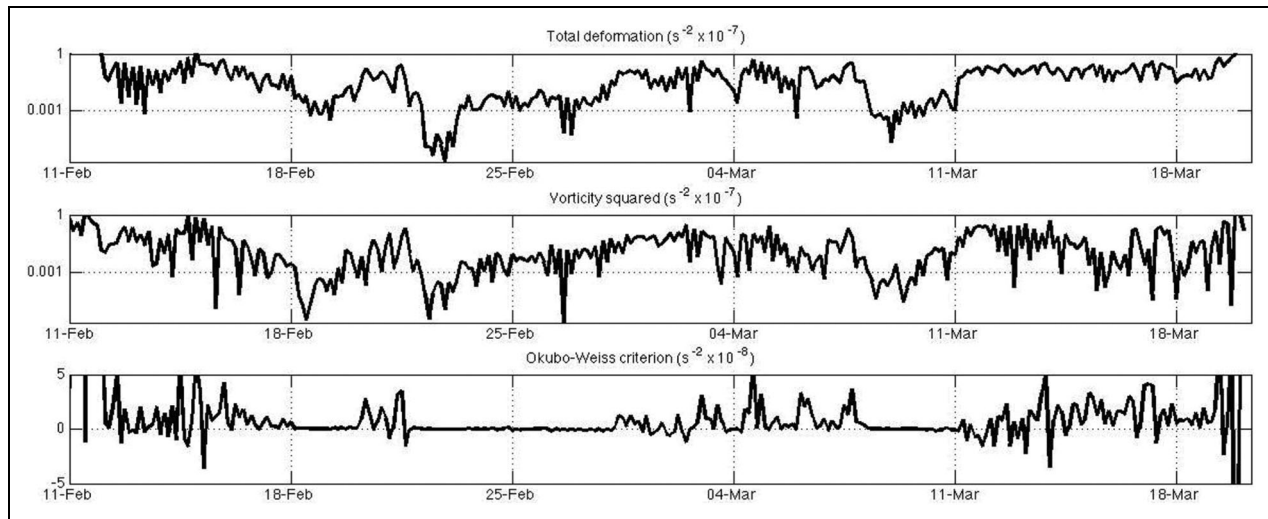
Figure 19. Relative differential kinematic parameters before, during, and after the extreme event of March 7–9, 2017. Parameters shown are (top to bottom) sea ice total deformation ($D^2 + S^2 + N^2$, where D indicates divergence, S indicates shearing deformation rate, and N indicates normal deformation rate, as shown in **Figure 18**), vorticity squared, and Okubo–Weiss criterion (relative contributions from vorticity and total deformation) before, during, and after the extreme blizzard event. Please see the text for more details on the determination of these parameters. DOI: https://doi.org/10.1525/elementa.2020.00128.f19

indicating enhanced deformation in the sea ice cover following the storm.

In summary, results from a Lagrangian dispersion analysis of ice beacons deployed in February and recording during the extreme event in March indicate distinct transitions in sea ice dynamical regimes before, during, and following the March 7–9, 2017, storm, characterized by temporal scaling maps depicting elliptic and advective, subdiffusive, and alternating sub- and super-diffusive regimes, respectively. Distinctive dynamical behavior is further reflected in DKPs and relative DKPs computed from the evolution in the triangular configuration of beacons that demonstrates sea ice deformation associated with stretching and shearing before the storm, comparable contributions during the storm, and enhanced deformation following the storm due to intermittent dominant contributions from vorticity and total deformation. This analysis provides a prescription for comparison between simulated and observed Lagrangian trajectories as the foundation for continued studies in understanding the impacts of extreme events on sea ice circulation in the HBC and as a contribution to ongoing development of an integrated observational-modeling Lagrangian framework to measure the ability of models to accurately capture sea ice dynamical features.

4. Synopsis

In this paper, we examined SSTs and sea ice conditions in the HBC as a baseline evaluation for the BaySys 2016–2018 field program time frame. The results from this study showed that SSTs were high in northwestern HB from May to July during the 2016–2018 time frame relative to the 1982–2010 climatology. Warmer SSTs were also observed throughout the annual cycle in both 2016 and 2017, with cooler SSTs observed throughout 2018. Similarly,

unusually low sea ice cover existed from August to December in 2016 and from July to September in 2017, while unusually high sea ice cover characterized January, February, and October of 2018. From an evaluation of freeze-up and breakup dates during the baseline years and in comparison with the 1981–2010 climatology, we found that the ice-free season was approximately 20 days longer in 2016 than in 2018, which was representative of the climatological mean. From an assessment of ice drift speeds and the meridional circulation index (MCI), we found strong circulation with a low ice cover (high SSTs) in 2016 and 2017 and weak circulation with high ice cover (low SSTs) in 2018. In keeping with past studies (i.e., Prinsenberg 1983), we observed high drift speeds and low MCI when river discharge to the HBC was high, illustrating local interactions. Contrasting MCI anomalies were reflected in contrasting SLP anomalies, illustrating regional interactions. In particular, unusually high ice drift speeds occurred in April of 2016 and 2017 and in May of 2018, coinciding with strong winds in 2016 and 2018 and zonal atmospheric flow in 2017. Unusually strong meridional circulation was observed in spring of 2016 and in September of 2017 during low river discharge conditions, and in December of 2017 during an anomalous SLP high/low regime to the northwest/southeast of the HBC. Weak meridional circulation existed in April of 2017 following the March 2017 blizzard, indicative of ice–ice interactions, and from January to April in 2018 when the HBC experienced low SSTs and high sea ice area.

In a case study of an extreme event, the blizzard of March 7–9, 2017, evaluated using Lagrangian dispersion statistics yielded temporal scaling exponent values characteristic of inertial oscillations superimposed on ice–ice, ice–coast interactions, and nonlocal transport just prior to the blizzard; a subdiffusive regime during the storm; and

combined super- and subdiffusive regimes following the storm characteristic of local and ice–ice and ice–coast interactions. The March blizzard was also shown to suppress sea ice deformation off the coast of Churchill, possibly due to refreezing in leads associated with a sudden drop in temperature. Results from this historical assessment and analysis are, in the context of a storylines approach (Shepherd et al., 2018), relevant to an investigation of possible future pathways and scenarios under continued climate change and river regulation. The Eulerian and Lagrangian diagnostics, tools, and framework developed here and in the companion paper (Lukovich et al., 2021) can be used as a foundation for a more permanent, integrated observational-modeling framework. Such a framework would allow for action on and response to relative climate change and river discharge regulation impacts on oceanographic and sea ice conditions in HB, relevant from the perspective of preparedness, adaptive management, and planning in a changing climate.

Data accessibility statement
The Optimum Interpolation sea surface temperature data were downloaded from //rda.ucar.edu/datasets/ds277.7/#!access. National Snow and Ice Data Center sea ice concentrations were downloaded from https://nsidc.org/data/G02202/versions/3. National Snow and Ice Data Center sea ice drift data, Version 4, were downloaded from https://daacdata.apps.nsidc.org/pub/DATASETS/nsidc0116_icemotion_vectors_v4/north/daily/.

Supplemental files
The supplemental files for this article can be found as follows:

Figures S1–S6. Equations. DOCX

Competing interests
The authors declare no competing interests.

Author contributions
Contributed to conception and design: JVL, SJ, AT.
Contributed to acquisition of data: SJ, JVL, DB.
Contributed to analysis and interpretation of data: JVL, SJ.
Drafted and/or revised the article: JVL, SJ, AT, PGM, JCS, KS, KW, DB, TAS, DGB.
Approved the submitted version for publication: All authors.

References
Artale, V, Calmanti, S, Carillo, A, Dell'Aquila, A, Herrmann, M, Pisacane, G, Ruti, PM, Sannino, G, Struglia, MV, Giorgi, F, Bi, X, Pal, JS, Rauscher, S. 2010. An atmosphere–ocean regional climate model for the Mediterranean area: Assessment of a present climate simulation. *Climate Dynamics* **35**: 721–740.

Banzon, V, Smith, TM, Chin, TM, Liu, C, Hankins, W. 2016. A long-term record of blended satellite and in situ sea-surface temperature for climate monitoring, modeling and environmental studies. *Earth System Science Data* **8**: 165–176. DOI: http://dx.doi.org/10.5194/essd-8-165-2016.

Bouillon, S, Rampal, P. 2015. Presentation of the dynamical core of neXtSIM, a new sea ice model. *Ocean Modelling* **91**: 23–37. DOI: http://dx.doi.org/10.1016/j.ocemod.2015.04.005.

Carmack, EC, Yamamoto-Kawai, M, Haine, TWN, Bacon, S, Bluhm, BA, Lique, C, Melling, H, Polyakov, IV, Straneo, F, Timmermans, M-L, Williams, WJ. 2016. Freshwater and its role in the Arctic Marine System: Sources, disposition, storage, export, and physical and biogeochemical consequences in the Arctic and global oceans. *Journal of Geophyical Research: Biogeosciences* **121**(3): 675–717. DOI: http://dx.doi.org/10.1002/2015JG003140.

Danielson, EW Jr. 1971. Hudson Bay ice conditions. *Arctic* **24**(2): 90–107.

De Szoeke, SP, Xie, SP. 2008. The tropical eastern Pacific seasonal cycle: Assessment of errors and mechanisms in IPCC AR4 coupled ocean-atmosphere general circulation models. *Journal of Climate* **21**: 2573–2590.

Environment and Climate Change Canada. 2020. Canadian climate normals 1981–2010. Available at https://climate.weather.gc.ca/climate_normals/index_e.html. Accessed 2 July 2021.

Francis, JA, Vavrus, SJ. 2015. Evidence for a wavier jet stream in response to rapid Arctic warming. *Environmental Research Letters* **10**(1): 014005. DOI: http://dx.doi.org/10.1088/1748-9326/10/1/014005.

Hochheim, KP, Barber, DG. 2010. Atmospheric forcing of sea ice in Hudson Bay during the fall period, 1980–2005. *Journal of Geophysical Research* **115**: C05009. DOI: http://dx.doi.org/10.1029/2009JC005334.

Hochheim, KP, Lukovich, JV, Barber, DG. 2011. Atmospheric forcing of sea ice in Hudson Bay during the spring season, 1980–2005. *Journal of Marine Research* **88**(3): 476–487.

Hutchings, JK, Roberts, A, Geiger, C, Richter-Menge, J. 2011. Spatial and temporal characterization of sea-ice deformation. *Annals of Glaciology* **52**: 360–368.

Ingram, RG, Prinsenberg, S. 1998. Coastal oceanography of Hudson Bay and surrounding eastern Canadian

waters, in Robinson, AR, Brink, KH eds., *The Global Coastal Ocean*. New York, NY: John Wiley: 105–133 (The Sea, vol. 11).

JafariKhasragh, S, Lukovich, JV, Hu, X, Myers, PG, Sydor, K, Barber, DG. 2019. Modelling sea surface temperature (SST) in the Hudson Bay Complex using bulk heat flux parameterization: Sensitivity to atmospheric forcing and model resolution. *Atmosphere-Ocean* **57**(2): 120–133. DOI: http://dx.doi.org/10.1080/07055900.2019.1605974.

Landy, JC, Ehn, JK, Babb, DG, Thériault, N, Barber, DG. 2017. Sea ice thickness in the Eastern Canadian Arctic: Hudson Bay Complex and Baffin Bay. *Remote Sensing of Environment* **200**: 281–294.

Lukovich, JV, Babb, DG, Barber, DG. 2011. Ice beacon trajectories in the Arctic during the IPY-CFL study. *Journal of Geophysical Research* **116**: C00G07. DOI: http://dx.doi.org/10.1029/2011JC007049.

Lukovich, JV, Geiger, CA, Barber, DG. 2017. Method to characterize directional changes in Arctic sea ice drift and associated deformation due to synoptic atmospheric variations using Lagrangian dispersion statistics. *The Cryosphere* **11**: 1707–1731. DOI: https://doi.org/10.5194/tc-11-1707-2017.

Lukovich, JV, Hutchings, JK, Barber, DG. 2015. On sea ice dynamical regimes in the Arctic Ocean. *Annals of Glaciology* **56**(69): 323–331.

Lukovich, JV, Tefs, A, Jafarikhasragh, S, Pennelly, C, Myers, PG, Stadnyk, TA, Sydor, K, Wong, K, Vieira, M, Landry, D, Stroeve, JC, Barber, DG. 2021. A baseline evaluation of atmospheric and river discharge conditions in the Hudson Bay Complex during 2016–2018. *Elementa: Science of the Anthropocene* **9**(1). DOI: http://dx.doi.org/10.1525/elementa.2020.00126.

Markham, WE. 1981. *Ice atlas of Canadian arctic waterways*. Toronto, Canada: Environment Canada Atmospheric Environment Service: 198.

Meier, WN, Fetterer, F, Savoie, M, Mallory, S, Duerr, R, Stroeve, J. 2017. *NOAA/NSIDC Climate Data Record of Passive Microwave Sea Ice Concentration, Version 3. Sea ice concentration*. Boulder, CO: National Snow and Ice Data Center. DOI: http://dx.doi.org/10.7265/N59P2ZTG. Accessed 10 February 2020.

Peng, G, Steele, M, Bliss, AC, Meier, WN, Dickinson, S. 2018. Temporal means and variability of Arctic sea ice melt and freeze season climate indicators using a satellite climate data record. *Remote Sensing* **10**(9): 1328. DOI: http://dx.doi.org/10.3390/rs10091328.

Prinsenberg, SJ. 1983. Effects of the hydroelectric developments on the oceanographic surface parameters of Hudson Bay. *Atmosphere-Ocean* **21**(4): 418–430. DOI: http://dx.doi.org/10.1080/07055900.1983.9649177.

Prinsenberg, SJ. 1984. Freshwater contents and heat budgets of James Bay and Hudson Bay. *Continental Shelf Research* **3**(2): 191–200.

Prinsenberg, SJ. 1986a. Salinity and temperature distribution of Hudson Bay and James Bay. *Elsevier Oceanography Series* **44**: 163–186.

Prinsenberg, SJ. 1986b. The circulation pattern and current structure of Hudson Bay. *Elsevier Oceanography Series* **44**: 187–204.

Prinsenberg, SJ. 1988. Ice-cover and ice-ridge contributions to the freshwater contents of Hudson Bay and Foxe Basin. *Arctic* **41**(1): 6–11.

Prinsenberg, SJ, Fowler, GA, van der Baaren, A. 1998. Pack ice convergence measurements by GPS-ARGOS ice beacons. *Cold Region Science and Technology* **28**(2): 59–72. DOI: https://doi.org/10.1016/S0165-232X(98)00013-5.

Prinsenberg, SJ, Freeman, NG. 1986. Tidal heights and currents in Hudson Bay and James Bay. *Elsevier Oceanography Series* **44**: 205–216.

Reynolds, RW, Smith, TM, Liu, C, Chelton, DB, Casey, KS, Schlax, MG. 2007. Daily high-resolution-blended analyses for sea surface temperature. *Journal of Climate* **20**: 5473–5496. DOI: http://dx.doi.org/10.1175/JCLI-D-14-00293.1.

Ridenour, NA, Hu, X, Jafarikhasragh, S, Landy, JC, Lukovich, JV, Stadnyk, TA, Sydor, K, Myers, PG, Barber, DG. 2019. Sensitivity of freshwater dynamics to ocean model resolution and river discharge forcing in the Hudson Bay Complex. *Journal of Marine Systems* **196**: 48–64.

Saucier, FJ, Senneville, S, Prinsenberg, S, Roy, F, Smith, G, Gachon, P, Caya, D, Laprise, R. 2004. Modelling the sea ice-ocean seasonal cycle in Hudson Bay, Foxe Basin and Hudson Strait, Canada. *Climate Dynamics* **23**: 303–326.

Shepherd, TG, Boyd, E, Calel, RA, Chapman, SC, Dessai, S, Dima-West, IM, Fowler, HJ, James, R, Maraun, D, Martius, O, Senior, CA, Sobel, AH, Stainforth, DA, Tett, SFB, Trenberth, KE, Van Den Hurk, BJJM, Watkins, NW, Wilby, RL, Zenghelis, DA. 2018. Storylines: An alternative approach to representing uncertainty in physical aspects of climate change. *Climatic Change* **151**: 555–571. DOI: https://doi.org/10.1007/s10584-018-2317-9.

Singh, RK, Maheshwari, M, Oza, SR, Kumar, R. 2013. Long-term variability in Arctic sea surface temperatures. *Polar Science* **7**(3–4): 233–240.

Stewart, DG, Lockhart, WL. 2005. An overview of the Hudson Bay marine ecosystem. Canadian Technical Report of Fisheries and Aquatic Sciences, No. 2586: 487. DOI: http://dx.doi.org/https://waves-vagues.dfo-mpo.gc.ca/Library/314704covermaterial.pdf.

St-Laurent, P, Straneo, F, Barber, DG. 2012. A conceptual model of an arctic sea. *Journal of Geophysical Research: Oceans* **117**(C6). DOI: http://dx.doi.org/10.1029/2011JC007652.

Tschudi, M, Meier, WN, Stewart, JS, Fowler, C, Maslanik, J. 2019. *Polar Pathfinder Daily 25 km EASE-Grid Sea Ice Motion Vectors, Version 4*. Boulder, CO: NASA National Snow and Ice Data Center Distributed Active Archive Center. DOI: http://dx.doi.org/10.5067/INAWUWO7QH7B. Accessed 9 August 2020.

ELEMENTA
Science of the Anthropocene

Elem Sci Anth is a peer-reviewed open access
journal published by University of California Press.

OPEN ACCESS